Advanced Electronic Materials

ADVANCED ELECTRONIC MATERIALS Open Access

www.advelectronicmat.de

RESEARCH ARTICLE OPEN ACCESS

All-Solution-Processed Perovskite Light-Emitting Transistors Enabled by a Fully Organic Architecture

Kelment Zahoaliaj[1] | Alice Fappani[2] | Francesca Pallini[2] | Valentina Bellotti[2] | Nicolò Quaresima[1] | Margherita Bolognesi[1] | Mario Prosa[1] | Luca Beverina[2] | Stefano Toffanin[1]

[1]Institute for the Study of Nanostructured Materials (ISMN), National Research Council (CNR), Bologna, Italy | [2]Department of Materials Science, University of Milano-Bicocca, Milano, Italy

Correspondence: Mario Prosa (mario.prosa@cnr.it) | Luca Beverina (luca.beverina@unimib.it) | Stefano Toffanin (stefano.toffanin@cnr.it)

Received: 6 October 2025 | **Revised:** 15 February 2026 | **Accepted:** 15 February 2026

Keywords: $CsPbBr_3$ | gate dielectrics organic light-emitting transistors | PeLETs | perovskite nanocrystals | solution processing

ABSTRACT

$CsPbBr_3$ perovskite nanocrystals (Pe-NCs) are promising solution-processable emitters for light-emitting devices due to their high brightness, color purity, and photoluminescence quantum yield. However, their integration into more advanced device architectures such as organic light-emitting transistors (OLETs) remains limited by the lack of fully solution-processable platforms that support uniform and compact Pe-NCs emissive layers (EMLs). In this work, we report fully solution-processed Pe-NCs-based LETs (Pe-LETs) using $CsPbBr_3$ nanocrystals as the emitter. The realization of such a device is enabled by the development of a fully organic LET platform that incorporates: (i) a tailored bilayer gate dielectric of polyvinyl alcohol (PVA) and CyTOP, (ii) a solvent-resistant p-type polymer semiconductor, poly[2,5-(2-octyldodecyl)-3,6-diketopyrrolopyrrole-alt-5,5-(2,5-di(thien-2yl)thieno[3,2-b]thiophene)] (DPP-DTT), and (iii) a nanocomposite EML of Pe-NCs dispersed in a poly(9-vinylcarbazole) and 1,3-bis[2-(4-tert-butylphenyl)1,3,4-oxadiazo-5-yl]benzene (PVK:OXD-7) matrix. Morphological and photophysical characterization, including confocal laser scanning microscopy, drives the optimization of solvent and processing conditions for uniform film formation. Benchmark device substructures are also used to fine-tune the organic platform for effective EML integration. The resulting Pe-LETs exhibit a narrow emission at 509 nm (full width at half maximum, FWHM = 19.2 nm), demonstrating excellent color purity suitable for displays and sensing. A maximum external quantum efficiency of 4.17×10^{-3} % is achieved, comparable to state-of-the-art values for inorganic-based LETs.

1 | Introduction

Organic light-emitting transistors (OLETs) are a class of optoelectronic devices that integrate electrical switching and amplification functions of organic field-effect transistors (OFETs) with the electroluminescence of organic light-emitting diodes (OLEDs). OLETs offer several attractive characteristics, including high charge-carrier mobility and current density, which are key enabling factors to generate high exciton densities and obtain devices with high brightness [1–4]. Their planar geometry allows tuning the location of the micrometer-sized emission zone within the transistor channel, making OLETs innovative light sources in integrated systems with multifunctional characteristics ideal for multidomain applications, from display technology to biodiagnostics [5–7]. However, despite their initial demonstration as innovative optoelectronic devices, OLET technology is still immature to enter the market due to limited performance in terms of electroluminescence efficiency [8]. Therefore, new design strategies and advanced materials are needed to unlock the full potential of OLETs as the next generation of low-cost and multifunctional electronic technology [9–12].

In this context, $CsPbX_3$ (X = Cl, Br, I) perovskite nanocrystals (Pe-NCs) are emerging materials that exhibit highly desirable emissive properties and can be effectively processed through solution-based methods [13–15]. Their photoluminescence (PL) is characterized by a wide color gamut obtained through the modulation of the Pe-NCs energy bandgap by: (1) changing the halogen ion, from chloride to bromide or iodide, or using different ratios of two or more halogens, (2) tuning the nanocrystal size to access quantum confinement effects [16]. The quantum confinement effect endows the Pe-NCs with narrow PL spectra having a full width at half maximum (FWHM) in the range 12–42 nm, and high photoluminescence quantum efficiencies (PLQY) approaching unity (100%) [17]. Considering these advantages, Pe-NCs have been used for a wide range of applications, from light-emitting diodes (LEDs) exhibiting bright and color-pure emission with external quantum efficiency (EQE) as high as 25.2% [18–23], to lasers [24], and light-emitting transistors [25–31].

In the literature, several Pe-NCs light emitting transistors (PeLETs) have been demonstrated by using oxide dielectrics and/or semiconductor layers that provide a robust yet inorganic architecture suitable for the deposition of the Pe-NCs [29–31]. The development of all-solution-processed LETs by using a fully organic platform is particularly attractive in view of the large-scale development of this technology, although it has been proven to be particularly challenging. In particular, the multilayered nature of the device architecture requires a fine control of all interfacial processes [32, 33] to ensure good charge mobility in the organic semiconductor (OSC) layer and efficient light-emission of the emissive layer (EML).

Herein, we present a fully solution-processed PeLET incorporating $CsPbBr_3$ NCs in the EML on a fully organic transistor platform, achieving a state-of-the-art EQE compared to PeLETs based on Pe-NCs with inorganic semiconductors [29].

To use Pe-NCs thin films as EMLs in electroluminescent devices, it is essential to ensure the formation of smooth and compact films [34, 35]. The presence of pinholes or an uneven distribution of NCs within the EML films can result in current leakage or high local current densities during device operation, affecting the electroluminescent efficiency. Chen et al., demonstrated that the solvent used to disperse the Pe-NCs can significantly impact the morphology of the films and the device performance, increasing the EQE of the PeLED by a seven-fold factor [36].

In this work, we tested dispersions of $CsPbBr_3$ Pe-NCs in four different solvents with different polarity (toluene, chlorobenzene, chloroform, and tetrahydrofuran). We carried out confocal laser scanning fluorescence microscopy (CLSM) and collected photoluminescence spectra and PLQYs to select the dispersing solvent leading to the Pe-NCs thin film with optimized morphology and optical properties.

Those properties can be further improved by realizing a nanocomposite thin film comprised of Pe-NCs and a suitable semiconducting polymer. The polymer matrix provides further degrees of freedom to improve solution-processability, film morphology, and electrical conductivity, while the Pe-NCs guest preserves its optical characteristics, which are dependent on their size, shape, and composition [27, 28, 37]. We implemented a multi-component strategy for the EML, consisting of mixing $CsPbBr_3$ NCs in a hole-transporting poly(9-vinylcarbazole) (PVK) matrix, while using an electron-transporting semiconducting molecule named 1,3-bis[2-(4-tert-butylphenyl)-1,3,4-oxadiazo-5-yl]benzene (OXD-7) to provide a suitable charge balance within the EML [38].

To obtain ideal interfaces and avoid any cross-contamination or mixed phases in the PeLET stack, we developed a robust, versatile and solution-processed device platform which integrates: (i) a bilayer gate dielectric composed of polyvinyl alcohol (PVA) and the fluoropolymer CyTOP, and (ii) the unipolar hole transporting semiconductor poly[2,5-(2-octyldodecyl)-3,6-diketopyrrolopyrrole-alt-5,5-(2,5-di(thien-2-yl)thieno[3,2-b]-thiophene)] (DPP-DTT). DPP-DTT is indeed a benchmark polymeric semiconductor that can achieve a high hole mobility up to 10.5 $cm^2\ V^{-1}\ s^{-1}$, [39] and it is resistant to many of the solvents in which the $CsPbBr_3$ Pe-NCs can be dispersed.

Eventually, fully-solution processed PeLETs were fabricated onto transparent glass substrate according to the following architecture: glass/ITO/PVA/ CyTOP/DPP-DTT/(Pe-NCs: PVK: OXD-7)/Ag. The resulting devices showed color-pure emission in the green range reaching a maximum EQE of 4.17×10^{-3}%, which demonstrates a performance consistent with state-of-the-art EQEs reported for inorganic Pe-NCs-based LETs [29].

2 | Results and Discussion

$CsPbBr_3$ NCs were synthesized according to the procedure we recently described in the context of composite materials for ionizing radiation detection [13, 40, 41]. Herein, we introduced an additional washing/reprecipitation step (Figure S1) to remove most of the excess oleylamine (OAm) ligand otherwise present on the nanocrystal surface. The presence of free OAm is not an issue for the optical applications, but negatively affects performance in optoelectronic devices. Indeed, OAm, acting as an insulating moiety on the NCs surface, hampers charge injection and transport. The presence of OAm on the surface is unavoidable for stability and processability, yet its amount must be reduced to the minimum to improve both charge-carrier injection and consequently exciton formation. Moreover, free OAm can form a salt with propionic acid, also employed in the synthesis of NCs. This leads to parasitic ionic currents and irreversible electrochemical reactions at the metal contacts when a voltage bias is applied. Finally, an excess of OAm can lead to the thermally-activated formation of non-luminescent, thermodynamically favored Cs_4PbBr_6 Pe-NCs [42].

Figure S2 shows the crystalline structure of the NCs before and after the purification step. X-ray diffractograms present a mixture of cubic and orthorhombic phases (equivalent in terms of optical properties), and the latter is more evident with the sharpening of the peaks due to the washing-induced NCs coalescence. Moreover, the diffractogram of washed NCs does not display spurious peaks. The effect of the purification step is also confirmed by the dramatic reduction of the ligand content from the thermogravimetric analysis (TGA) (Figure S3), estimated with the total loss at 450°C. The weight loss normally occurs in two steps, with the first one attributed to the external shell of free amine and the second one to the protonated ligand directly bound

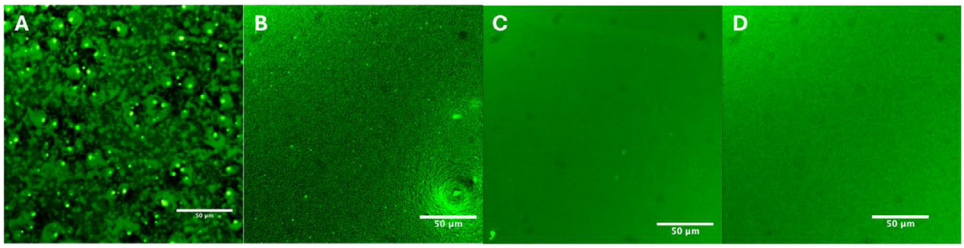

FIGURE 1 | CLSM 200 × 200 µm-wide images (excitation 488 nm, spectral recollection 500–530 nm) Pe-NCs films spin-coated from the dispersion of the NCs in different solvents: (A) Toluene, (B) Chlorobenzene, (C) Chloroform, and (D) Tetrahydrofuran.

TABLE 1 | Summary of the PLQY of the Pe-Ncs films (excitation at 390 nm).

Solvent	Toluene	Chlorobenzene	Chloroform	Tetrahydrofuran
PLQY[a]	5.5%	4.5%	3.0%	12.9%
Abs[b]@390 nm [A.U.]	0.16	0.16	0.28	0.25

[a]phospholuminescence quantum yield.
[b]absorption.

to the NCs surface. The washing step mainly removes the outer and weakly interacting shell.

To identify the most suitable processing solvent, $CsPbBr_3$ NCs were re-dispersed in four solvents with different physicochemical characteristics: toluene, chlorobenzene, chloroform, and tetrahydrofuran. CLSM was used to investigate the thin-film quality, in terms of morphology and photoluminescence characteristics, of $CsPbBr_3$ NCs spin-coated onto glass (Figure 1).

In Figure 1A, the film prepared using toluene displays a non-uniform emission, characterized by micrometer-sized luminescent aggregates, with lateral dimensions of around 4–5 µm, surrounded by a non-emissive background. The uneven spatial distribution of domains in the solid state may arise from a suboptimal dispersion of Pe-NCs in toluene as well as from the unfavored wetting of the substrate, hindering uniform film formation. In comparison, the use of a solvent with slightly higher polarity, like chlorobenzene, produces a film (Figure 1B) with reduced inhomogeneity, observed on a smaller length scale. Aggregates are in the range from sub-micrometer to 1 µm, with only a few aggregates reaching 10 µm of lateral size.

In contrast, the films obtained from chloroform and tetrahydrofuran (Figure 1C,D) show a more uniform fluorescence intensity over the entire scanned region, and the absence of aggregated structures. These observations suggest that the higher polarity of chloroform and tetrahydrofuran is a key factor in dispersing the $CsPbBr_3$ NCs. Indeed, chloroform and tetrahydrofuran have a polarity index P' (Snyder's Polarity Index) of 4.1 and 4.0, respectively, against 2.4 and 2.7 for toluene and chlorobenzene, respectively. Besides polarity, the solvents' coordination capability and vapour pressure also influence the film's morphology and emission.

Table 1 reports the PLQY values obtained by exciting the four Pe-NCs films at 390 nm, which corresponds to a peak/shoulder of the absorption spectrum of Pe-NCs solutions [13]. The films deposited from toluene and chlorobenzene show PLQY values as low as 5.5% and 4.5% (Table 1), respectively, indicating that the inhomogeneous nanocrystal distribution negatively impacts the photoluminescent properties of the $CsPbBr_3$ thin films. Counter-intuitively, the chloroform-based film (Table 1) exhibits an even lower PLQY (3.0%) despite the higher degree of homogeneity. Instead, the tetrahydrofuran-based film shows the highest PLQY of 12.9% [43]. This difference in the PLQY values between the two polar solvents could be attributed to a more efficient surface passivation of the Pe-NCs by tetrahydrofuran. While both solvents can induce the ligand removal from the Pe-NCs surface, the oxygen atom in the tetrahydrofuran molecule can coordinate the Pb^{2+} centers, forming Pb-O interactions, which could increase the passivation of the Pe-NCs as typically occurring with aprotic polar solvents, such as DMF and DMSO [44]. Consequently, tetrahydrofuran was chosen as the primary solvent for dispersing Pe-NCs, as it achieves a significantly enhanced photoluminescence performance.

Films obtained by spin coating the Pe-NCs dispersed in the four different solvents are all thinner than 10 nm. Typically, a layer-by-layer deposition approach is adopted with Pe-NCs to achieve a film thickness suitable for use as an EML in a device [45]. However, the attempt to implement multiple coating steps introduced additional inhomogeneities (data not shown), which made $CsPbBr_3$ films poorly compatible with device application. Consequently, to obtain a thicker and uniform EML film, a polymeric matrix was used as a dispersing agent of $CsPbBr_3$ NCs. PVK, a known hole-transporting semiconducting polymer [46], is widely recognized for its excellent film-forming properties and has been frequently employed as a host in the EML of OLEDs. The energy levels of the Pe-NCs (i.e., their highest occupied molecular orbital, HOMO, and lowest unoccupied molecular orbital, LUMO) are located within the HOMO–LUMO gap of PVK (Figure S4). This energy-level alignment is expected to favor charge transfer, and consequently

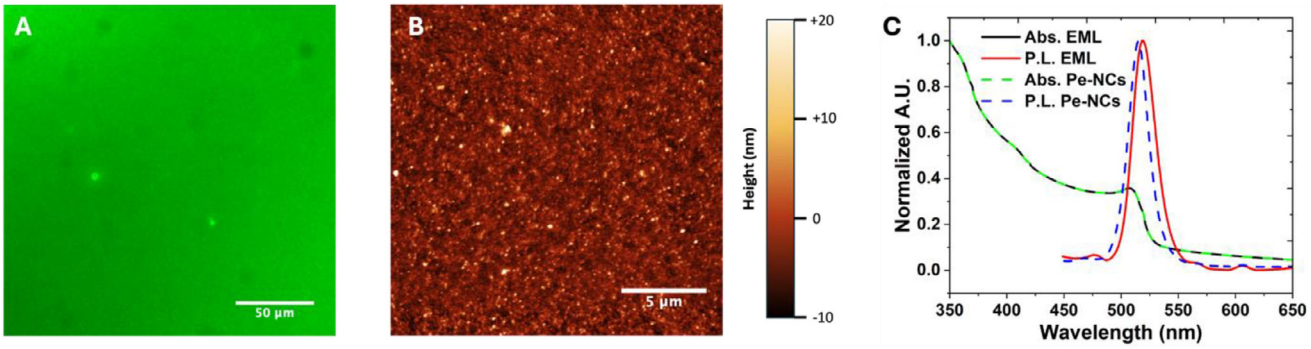

FIGURE 2 | (A) CLSM (excited at 488 nm), (B) AFM images and (C) normalized absorption and photoluminescence spectra of Pe-NCs and Pe-NCs: PVK: OXD-7 (1: 0.7: 0.3) films.

recombination, from PVK matrix to Pe-NCs. However, to achieve efficient electroluminescence (EL), a well-balanced injection of both opposite charges into the Pe-NCs is required. To achieve this in the EML, an electron-transporting material (ETM) such as the most reported in literature, OXD-7, was introduced in a blend with PVK. As in the case of PVK, the HOMO and LUMO levels of the Pe-NCs are situated within the energy gap of the HOMO and LUMO levels of OXD-7. To note, both host materials are readily soluble in tetrahydrofuran, the solvent previously identified as the optimal option for dispersing the Pe-NCs.

According to a previous study by our group [47], the ratio between PVK and OXD-7 was set to 7:3 (w/w) to guarantee an efficient charge balance within the EML. Based on the work of A. N. Aleshin et al., a total ratio of 1:1 was selected for the EML matrix $CsPbBr_3$ Pe-NCs blend, resulting in an EML composition of 1:0.7:0.3 for Pe-NCs, PVK, and OXD-7, respectively [28]. Overall, the Pe-NCs-based nanocomposite approach allowed for obtaining an EML film thickness in the range from tens to hundreds of nm, which is also suitable for LET implementation.

The morphological and optical properties of the optimized EML based on the selected nanocomposite were examined in more detail by CLSM and atomic force microscopy (AFM) (Figure 2A,B). The CLSM image, collected under the same excitation conditions used for the neat Pe-NCs films, demonstrates a uniform emission across the scanned area of the nanocomposite EML, similar to what was observed in the tetrahydrofuran-based Pe-NCs films (Figure 1D). The AFM characterization revealed a root mean square (RMS) roughness of approximately 3.74 nm, highlighting the smoothness of the blend surface. Figure 2C compares the absorption and PL spectra of the composite film with those of the neat Pe-NCs film. The absorption profiles of both samples are nearly identical, indicating negligible contributions from either PVK or OXD-7 in the visible range. Under 390 nm excitation, the PL emission peak remains centered at ~516 nm with a FWHM of ~23 nm, confirming that the polymer matrix does not alter the radiative properties of the Pe-NCs.

However, the PLQY of the EML blend is 4.13%, which is lower than that of the neat Pe-NC film. This reduction might be attributed to additional nonradiative decay pathways related to multiple interfaces present in the nanocomposite film.

The Pe-NCs:PVK:OXD-7 blend was evaluated as EML in a standard PeLED architecture (Figure S5) for a preliminary investigation of the capability of the nanocomposite to generate light under voltage bias. Devices showed good diode-like electrical characteristics and a maximum optical power output of 2.92 µW (Figure S6), highlighting the efficient optoelectronic operation of the EML. Although the device structure could be optimized in terms of performance, the simple and solution-processable benchmark architecture allowed to assess the EML operation before the implementation in a more complex transistor platform.

To develop a multilayered architecture for the OFET displaying resistance to the processing solvent for the Pe-NCs (tetrahydrofuran), the first step was identifying a suitable insulating polymer as the gate dielectric. Polyvinyl alcohol (PVA), poly(vinylidene fluoride-trifluoroethylene-chlorofluoroethylene) (PVDF-TrFE-CFE), and the fluoropolymer CyTOP were tested. The choice of these materials arises from their promising dielectric characteristics in conjunction with their possible compatibility with the Pe-NCs deposition. PVDF-TrFE-CFE, for instance, is well-known for its high dielectric constant, which enables the fabrication of OFETs with low threshold voltages (V_{th} < −5 V) [48]. On the other hand, PVA has a lower dielectric constant compared to PVDF-TrFE-CFE but offers an excellent balance between dielectric properties, mechanical flexibility, and processability into thin films with minimal free volume [49, 50]. CyTOP has an even lower dielectric constant but is the most resistant to solvents among all the polymers mentioned above. All polymers were processed into thin films and subjected to a tetrahydrofuran washing by solvent spin coating. As resulting from an eye inspection and profilometry (data not shown), the PVA and CyTOP films remained intact and unaffected by the solvent washing, whereas PVDF-TrFE-CFE films degraded significantly. Consequently, PVA and CyTOP were selected as the dielectric materials for further development.

The semiconductor material selected was DPP-DTT, a hole-transporting semiconducting polymer that can be solution-processed in chlorinated solvents, making it compatible with both of the dielectric polymers.

The OFETs fabricated as test devices (Figure S7) comprise an ITO gate electrode, an insulating layer of either PVA or CyTOP, DPP-DTT as the OSC, and Ag drain and source electrodes. However, both devices demonstrated unsatisfactory performance as OFETs.

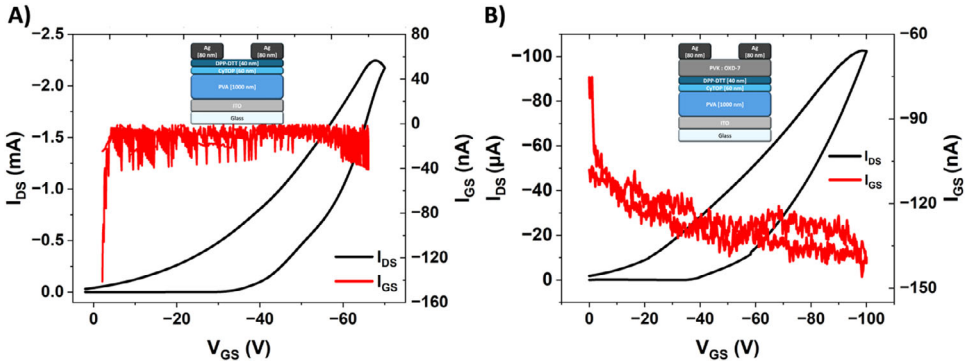

FIGURE 3 | (A) Device structure of OFET-1 and P-type saturation transfer curve at $V_{DS} = -100$ V collected both in forward and backward scan; (B) Device structure of OFET-2 and P-type saturation transfer curve at $V_{DS} = -100$ V collected both in forward and backward scan.

The device with CyTOP as the dielectric exhibited poor electrical properties. From the transfer p-polarized characteristic (Figure S7A), the low source-drain current (I_{DS}) (around 100 μA) was correlated to the low hole mobility inherent to the low dielectric-constant polymer used. Moreover, the non-negligible gate-source current (I_{GS}) (around 17 μA) indicates leakage through the insulating layer. The possibility of using a thicker layer of CyTOP to reduce the I_{GS} leakage was discarded because the thicker layer would increase the gated threshold and thus the operational bias. Similarly, the device with PVA as the insulator also displayed poor electrical performance, likely due to the contribution of residual ionic currents from the PVA layer (Figure S7B) [51]. The use of a double-layer dielectric made of PVA/CyTOP was then considered. The rationale behind this strategy was to use the PVA to provide a relatively high dielectric-constant material and the CyTOP to provide a barrier interface between the PVA and the DPP-DTT to limit the ionic current contribution. Indeed, H. Chen et al. have very recently demonstrated a highly efficient flexible OLET using PVA and CyTOP as bilayer dielectrics [49]. Following this approach, dielectric films were fabricated using PVA (1000 nm) as the bottom dielectric layer, and CyTOP (60 nm) as the top dielectric layer, and the overall dielectric characteristics of the bilayer were evaluated in a capacitor device (Figure S8A). Figure S8B shows the capacitance-frequency response of the PVA/CyTOP dielectric system measured across a frequency range of 1 Hz to 10 kHz. The calculated capacitance per unit area (C_i) at 20 Hz of the PVA/CyTOP bilayer dielectric resulted in 5.93 nF/cm^2. This frequency value was used for calculating charge mobility because the impedance phase is approximately 85°, thus close to the ideal capacitive value of 90° (Figure S8C), while the contribution to polarization of the dielectric by the mobile ions (inherently present in the PVA layer) is reduced. The content of ionic species in the PVA layer can be related to the aqueous processing route of the thin film and residual synthesis-related impurities, such as Na^+ ions.

The fabricated OFET structure (OFET-1), incorporating the bilayer gate dielectric PVA/CyTOP and the organic semiconductor DPP-DTT, showed good saturation transfer characteristics (Figure 3A), which revealed a maximum current of approximately 2.3 mA, a hole mobility (μ_h) of 1.69 cm^{2}V^{-1}s^{-1} and a threshold voltage (V_{th}) of −12.7 V. Although the transfer characteristics show a non-negligible hysteresis likely due to residual ionic mobility of PVA, the device performance is in line with the best results found in literature for DPP-DTT, thus indicating strong charge transport properties and efficient operation of the OFET [52].

To simulate the integration of the EML and test the solvent resistance of the organic platform, an OFET named OFET-2 was fabricated by depositing the host matrix blend (PVK:OXD-7, without Pe-NCs) onto the PVA/CyTOP/DPP-DTT structure (Figure 3B). The addition of the host matrix layer resulted in a decrease of the maximum I_{DS} current, as expected, due to the additional resistance to charge injection and extraction given at the source/drain electrodes [53]. The low hole mobility of PVK likely contributed to the reduction in total I_{DS} current. Nevertheless, the device showed an I_{on}/I_{off} ratio of approximately 10^3 and a μ_h of 3.27×10^{-2} cm^{2}V^{-1}s^{-1}. Both OFET-1 and OFET-2 exhibit no relevant light emission. These results demonstrate the feasibility of integrating the host matrix layer into the PeLET structure while maintaining functional transistor behavior.

As shown in Figure 4A, the complete PeLET structure was successfully fabricated by depositing the nanocomposite EML onto the fully organic device structure. The energy diagram of the device (Figure 4B) illustrates the suitable energy level alignment of the active materials within the PeLET. When source-drain and source-gate voltage potentials are applied, the holes accumulate at the DPP-DTT/dielectric, flow in the hole-transporting semiconductor, and then are injected into the PVK's HOMO level and eventually transferred into the Pe-NCs' HOMO level. At the proper bias conditions, electrons are injected from the OXD-7's LUMO level into the Pe-NCs' LUMO level, thus allowing exciton formation and consequently photon emission.

Figure 4C–F reports the full optoelectronic characterization of PeLET devices. Figure 4C shows the p-polarized saturation transfer characteristics of PeLETs, which show emission of light with a maximum optical power output of 19.9 nW achieved at a drain current of 197 μA (Table 2). The electroluminescence (EL) spectrum of the PeLET device reported an emission peak centered at 509 nm, with a FWHM of 19.2 nm (Figure 4D). This sharp emission peak is characteristic of $CsPbBr_3$ Pe-NCs and indicates that the radiative recombination predominantly occurs within the Pe-NCs. Additionally, the overlapping PL and EL spectra of Pe-NCs dissolved in tetrahydrofuran (Figure 2C) and of the device with Pe-NCs-based nanocomposite (Figure 4D), respectively,

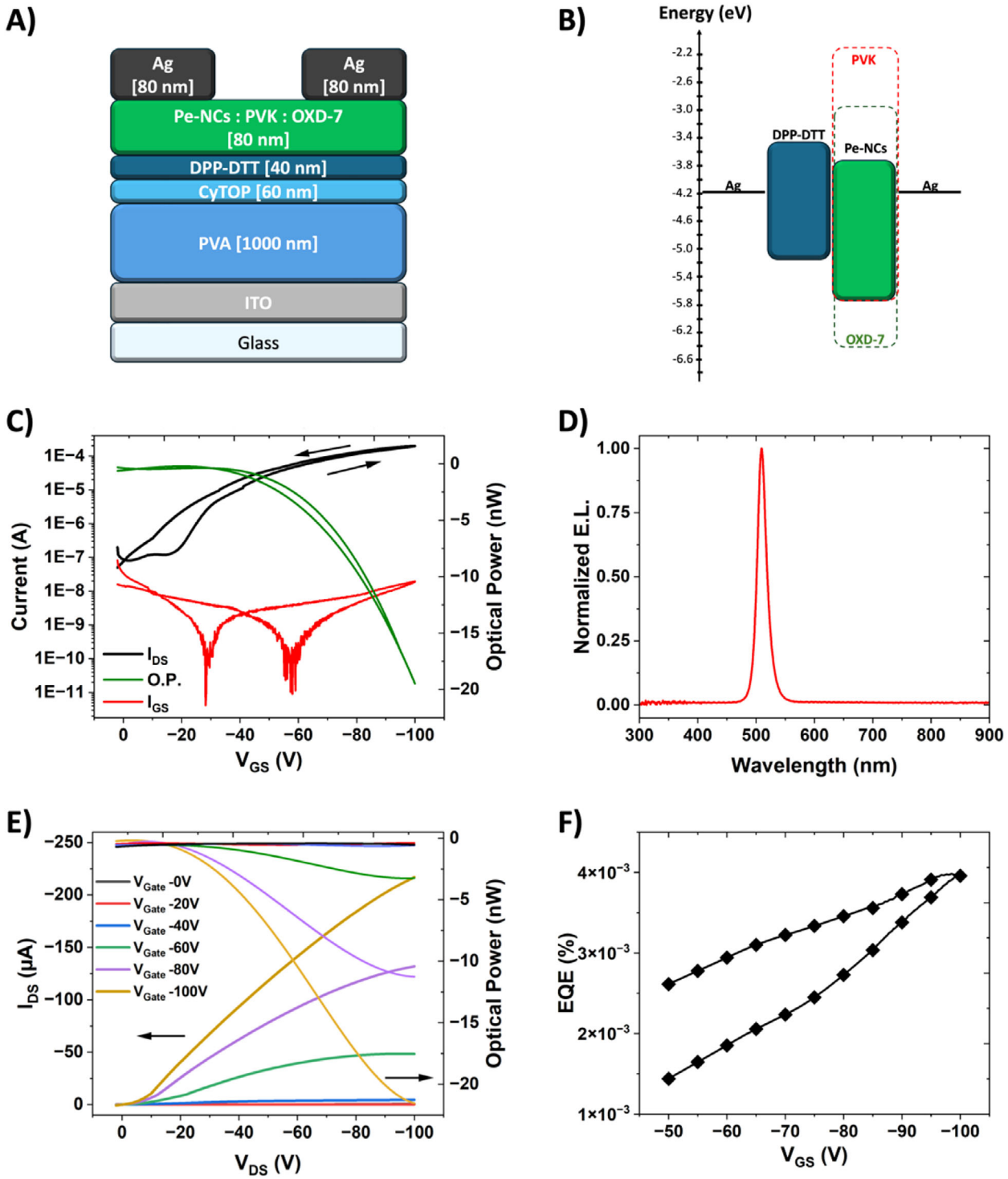

FIGURE 4 | (A) Device structure of PeLET; (B) Energy level diagram (HOMO and LUMO) of the materials; (C) P-type saturation transfer curve at $V_{DS} = -100$ V collected both in forward and backward scan; (D) Electroluminescence spectrum of PeLET (E) Output curves recorded at V_{GS} ranging from 0 to −100 V; (F) EQE% curve calculated from the P-type saturation transfer curve (C).

suggest minimal impact from the surrounding matrix and device architecture on the optical properties of the emissive material. Figure S9 shows the image of the light emission zone in the device active region collected at unipolar bias conditions, where the EL intensity is maximized: as expected, the light emission zone is completely located underneath the drain electrode, where brighter sub-micrometric grain-like emissive spots are visible.

Figure 4E presents the p-polarized multiple output characteristics of the PeLET, where a clear saturation regime is reached at gate voltages below −60 V. When compared to the OFET-2 (ITO/PVA/CyTOP/DPP-DTT/(PVK:OXD-7)/Ag), PeLETs exhibit significant enhancements in key performance parameters. The drain current increases by approximately 95 μA, and the hole mobility is nearly twice as high in the PeLET 6.04 × 10^{-2}

TABLE 2 | Summary of the main figures of merit of OFETs and PeLET calculated from the transfer P-type characteristic.

Device	I_{DS}[a] (μA)@V_{GS} max	I_{GS}[b] (nA)@V_{GS} max	I_{DS}/I_{GS}	I_{on}/I_{off}[c]	V_{Th}[d] (V)	μ_{Hole}[e] ($cm^2 V^{-1} s^{-1}$)	Power (nW)	EQE[f] (%)
OFET-1	2270	40	5.7E04	10^3	−12.7	1.69	—	—
OFET-2	102	139	734	10^3	−12.7	3.27E-02	—	—
PeLET	197	20	9.9E03	10^4	−17.0	6.04-02	19.9	4.17E-03

[a]Drain-source current.
[b]Gate-source current.
[c]Ratio of on and off current.
[d]Threshold gate voltage.
[e]Hole mobility.
[f]External quantum efficiency.

$cm^2V^{-1}s^{-1}$ compared to the 3.27×10^{-2} $cm^2V^{-1}s^{-1}$ observed in OFET-2 (Table 2). To note, the incorporation of Pe-NCs in the EML matrix significantly reduced the electrical hysteresis observed in the p-polarized saturation transfer characteristics. It is likely that the polarization induced by the ionic moieties in the Pe-NCs dispersed in the EML may counterbalance the ionic diffusion ascribed to PVA.

These improvements highlight the role of the Pe-NCs within the EML in enhancing device performance. Beyond serving as the emissive material, the Pe-NCs appear to facilitate charge injection and recombination within the device. This dual functionality likely reduces the energy barriers at material interfaces and contributes to a better charge balance in the device, leading to increased current, higher mobility, and a lower threshold voltage.

The structural integration of Pe-NCs into the PVK:OXD-7 matrix is particularly significant, as it establishes a synergistic interaction between the charge transport layers and the emissive material, highlighting the importance of material engineering in achieving good PeLET performance.

The calculated EQE% as a function of applied voltage (Figure 4F) shows a maximum value of 4.17×10^{-3}%. To the best of our knowledge, this value is consistent with the state-of-the-art EQEs obtained for LET devices based on an inorganic FET platform [29]. Although further improvement of the device performance is still needed for practical applications, the development of a fully solution-processed PeLET with narrow emission color and compatible with scalable techniques could favor the industrial exploitation of the technology.

3 | Conclusion

To summarize, in this study, we successfully developed all solution-processed multilayer PeLETs using $CsPbBr_3$ Pe-NCs as the emissive material on a fully organic transistor platform. The optimization of the Pe-NC thin-film morphology in various solvents and the implementation of a nanocomposite approach for the EML led to uniform and high-quality films, which is a key-enabling factor in the realization of scalable, low-cost, and efficient solution-processed optoelectronic devices. By using designed diode-like devices and transistor sub-structures, (i) the EML was systematically optimized to provide balanced charge transport and optimal optical properties, and (ii) the accessibility and functionality of the fully-organic platform were optimized and tested to support the solution-processed Pe-NCs EML. The resulting PeLET devices showed state-of-the-art optoelectronic characteristics, such as external quantum efficiency (EQE) of 4.17×10^{-3} and optical power output of 19.9 nW, with a narrow emission peak at 509 nm and a FWHM of 19.2 nm, indicating a high color purity. This work demonstrates the feasibility of fully solution-processed PeLETs, paving the way for their application in advanced optoelectronic systems, including displays and optical sensors.

4 | Experimental Section

4.1 | Chemicals

Cesium carbonate (Cs_2CO_3, 99%) and lead(II) bromide ($PbBr_2$, 99%) were purchased from Fluorochem. Propionic acid (PA, 99%) and oleylamine (OAm, 80%) were provided by Thermo Fisher, and tetrabutylammonium bromide (TBAB, 98%) was purchased from BLDpharm. Isopropanol (99.8%), heptane (Hept, 99%), and toluene (99.8%) were all provided by Carlo Erba. Isopropanol was distilled from CaH_2 before use. All the other chemicals were used as received.

4.2 | Synthesis and Washing of $CsPbBr_3$-OAm Pe-NCs

The OAm-capped $CsPbBr_3$ NCs were synthesized by adapting a previously described protocol from Mecca et al. (2023) [39] to a 1.8 L scale (referred to the Cs^+ precursor solution), yielding 3.2 g of raw NCs. In particular, the precursor solutions were mixed under turboemulsification (the turboemulsifier homogenizer was bought from IKA and consists of a motor group T50 digital Ultra Turrax and a dispersing tool with code S50N-G45 M), and 900 mL of isopropanol was added to the raw clear dispersion to induce precipitation before centrifuging and drying. The washing was performed on 500 mg of dried NCs, suspending in 100 mL of toluene (5 mg/mL) and stirring overnight. 50 mL of isopropanol was added, and after 3 h of further stirring, the solid was recovered by centrifuging at 4500 rpm for 15 min and dried to yield 297 mg (59.4%) of washed NCs as an orange powder.

4.3 | Powder X-Ray Diffraction (PXRD) Measurements

The materials were characterized with a Rigaku MiniFlex 600 instrument operating at 45 kV and 40 A with a copper radiation source (Kα 1.54). The diffractograms were collected in a laboratory atmosphere at room temperature from 5° to 50°, with steps of 0.02° and a scanning speed of 3 deg/min. The samples were prepared by drop-casting a dispersion of the NCs (50 mg/mL) on glass slides for the as-synthesized material and pressing the powder on the sample holder for the washed NCs.

4.4 | Thermogravimetrical Analysis (TGA)

The measurements were performed on a TGA/DSC STARe System (Mettler Toledo). The method goes from 30°C to 600°C with a heating rate of 10°C/min, under a nitrogen flux of 50 mL/min. Solid state samples (10–15 mg) were loaded in Al_2O_3 crucibles.

4.5 | Pe-NCs Thin Films Preparation

The Pe-NCs were dispersed in the four solvents (Sigma-Aldrich) at a concentration of 10 mg/mL and sonicated for 1–2 h. First, the glass substrates were sequentially cleaned in a sonication bath twice with acetone for 15 min each and once with isopropanol for 15 min, then dried with an argon flow. The prepared dispersions were spin-coated onto the cleaned glass substrates at 1000 rpm, 1000 rpm/s for 1 min.

4.6 | EML Thin Film Preparation

The solution of the EML was prepared by dispersing the Pe-NCs (8.35 mg/mL) in a solution of PVK (Thermo Scientific, 90 kDa) (5.55 mg/mL) and OXD-7 (Ossila) (2.40 mg/mL) in tetrahydrofuran. The solution was spin-coated onto the cleaned glass substrate (cleaned as mentioned above) at 3000 rpm, 3000 rpm/s for 1 min.

4.7 | Laser Scanning Confocal Microscopy

The LSCM images of all thin films prepared as described above were acquired using a Nikon TE2000 optical microscope equipped with a 60 × objective lens with a numerical aperture of 0.70. The microscope was connected to a Nikon EZ-C1 confocal scanning head for high-resolution imaging. The films were excited with a laser at a wavelength of 488 nm, and the dichroic used for the measurement was 488/543.

4.8 | Absorption and Photoluminescence Measurements

The UV–vis absorption spectra of the Pe-NCs and EML thin films were obtained with a Jasco V-550 UV–vis spectrophotometer, while the PL spectra were obtained with an Edinburgh Instruments FS5 spectrofluorometer by exciting the samples at 390 nm. PLQY was calculated by the software of an Edinburgh Instruments FS5 spectrofluorometer equipped with an integrating sphere, from the elaboration of the spectra collected for a reference bare glass side, and a glass slide coated with the Pe-NCs thin films. The absorbed light was calculated as the difference between the integrals of the excitation light spectra after impinging on the reference and on the sample. The emission light was calculated as the difference between the integrals of the emission spectra of the Pe-NCs films and the reference sample. The PLQY was then calculated as the ratio between emitted and absorbed light.

4.9 | Atomic Force Microscopy

Topographic AFM measurement of the EML film was performed in Tapping mode using MikroMasch HQ:NSC35/Al BS probes with a nominal spring constant of 5.4 N m^{-1} and tip radius < 8 nm on NT-MDT Smena microscope head. All measurements were performed in the air. Background correction and image analysis were performed with Gwyddion v2.66.

4.10 | Devices Fabrication

The PeLET devices were fabricated in a bottom-gate/top-contact configuration on 25 × 25 mm transparent glass/ITO substrates. On top of the substrates (cleaned as mentioned above), a layer of PVA (VWR Chemicals) was deposited by spin-coating a 10% (w/w) solution of PVA in water at 8000 rpm for 60 s and annealed overnight at 105°C in a vacuum oven. Then a solution of CyTOP (AGC, CTL-809 M) diluted 1:2 with its proprietary solvent (AGC, CT-SOLV180) was spin-coated at 7000 rpm for 45 s and annealed for 2 h at 105°C in a vacuum oven. A soft plasma treatment (10 s, 50 W) was applied to the CyTOP layer. The DPP-DTT semiconductor solution of 4 mg/mL in chloroform was spin-coated at 1000 rpm for 60 s and annealed at 160°C for 30 min on a hot plate. The solution of the EML prepared as above was spin-coated at 3000 rpm, 60 s. The organic stack was covered by 80 nm thick silver source and drain electrodes deposited by thermal evaporation at 1.0 Å sec^{-1}. The metal electrodes were deposited using shadow masks in a homemade high-vacuum deposition chamber at a base pressure of 10^{-7} mbar. The resulting devices presented the following geometrical characteristics: 70 μm channel length (L), 12 mm channel width (W), and 500 μm wide source and drain electrodes.

For OFET-1 the procedure is the same except for the EML deposition step. For OFET-2, instead of the deposition of the EML, a solution of PVK (5.55 mg/mL) and OXD-7 (2.40 mg/mL) in THF was spin-coated at 3000 rpm for 60 s.

For the capacitor devices, the PVA and CyTOP layers were deposited as above on top of a cleaned glass/ITO substrate. Then a square 1.2 x 1.2 cm silver electrode was deposited on top with the same conditions as above.

4.11 | Optoelectronic Characterization of OFETs and PeLETs

The electrical and optical measurements of the OFETs and PeLETs were performed in an inert atmosphere inside a nitrogen-filled glovebox using a standard SUSS probe station coupled

to a B1500A Agilent semiconductor device analyzer. The light output was measured at the bottom side of the substrates with a silicon photodiode (sensitivity of 0.38 A W^{-1} at 600 nm) directly in contact with the devices. PeLET steady state EL spectrum was obtained by collecting the signal with a Hamamatsu PMA optical multichannel analyzer. The field-effect mobility in the saturation regime (μ) was calculated using the equation $I_{DS} = (W/2L)C_i\mu(V_{GS} - V_{Th})^2$, (Figure S10) where C_i is the capacitance per unit area of the insulating layer and V_{Th} is the threshold voltage extracted from the square root of the drain current ($I_{DS}^{1/2}$) vs. gate voltage (V_{GS}) characteristics.

Optical microphotographs of the PeLET active region were taken with a Nikon TE-2000 inverse microscope using a sample holder equipped with electrical connections. Optical detection was achieved using 60 × magnification air-objectives and a Hamamatsu ORCA high-sensitive digital camera.

4.12 | Impedance Measurement of the Capacitor and Capacitance Calculation

The measurement of the impedance was performed in a laboratory atmosphere using Autolab electrochemical station. The capacitance (C) was calculated using the equation $C = -1/2\pi fZ''$, where f is the frequency and Z″ is the imaginary part of the impedance. The C_i was calculated with the equation $C_i = C/A$ where A is the area of the capacitor.

Acknowledgements

The authors thank Francesco Reginato and Particular Materials srl for the fruitful scientific discussion and Salvatore Moschetto, Federico Prescimone, Vincenzo Ragona, Federico Bona, and Tiziano Bonfiglioli for the technical support. This work received funding from the European Union's Horizon Europe Research and Innovation Programme under grant agreement 101157922 (ESPFdigit). This work was supported by the project "Inorganic and Sustainable Metal-halide perovskite Nanocrystals for LIGHT emission—ISMN LIGHTS" funded by the Institute of Nanostructured Materials (ISMN) of the Italian Research National Council (CNR).

Funding

European Union's Horizon Europe Research and Innovation Programme under grant agreement 101157922 (E-SPFdigit)

Conflicts of Interest

The authors declare no conflicts of interest.

Data Availability Statement

The data that support the findings of this study are available from the corresponding author upon reasonable request.

References

1. C. Zhang, P. Chen, and W. Hu, "Organic Light-Emitting Transistors: Materials, Device Configurations, and Operations," *Small* 12 (2016): 1252–1294, https://doi.org/10.1002/smll.201502546.

2. X. Li, Z. Wu, W. Peng, et al., "UV/Ozone-Induced Interface Engineering for High-Performance Horizontal Organic Light-Emitting Transistors Operating at Low Voltage," *Small* 21 (2024): 2407019, https://doi.org/10.1002/smll.202407019.

3. H. Huang, Z. Miao, H. Gao, et al., "High-Performance Stable Hybrid Inorganic-Organic Light-Emitting Transistor," *SmartMat* 6 (2025): 1321, https://doi.org/10.1002/smm2.1321.

4. W. A. Koopman, M. Natali, G. P. Donati, M. Muccini, and S. Toffanin, "Charge–Exciton Interaction Rate in Organic Field-Effect Transistors by Means of Transient Photoluminescence Electromodulated Spectroscopy," *ACS Photonics* 4 (2017): 282–291, https://doi.org/10.1021/acsphotonics.6b00573.

5. M. Prosa, S. Moschetto, E. Benvenuti, et al., "2,3-Thienoimide-Ended Oligothiophenes as Ambipolar Semiconductors for Multifunctional Single-Layer Light-Emitting Transistors," *Journal of Materials Chemistry C* 8 (2020): 15048–15066, https://doi.org/10.1039/d0tc03326j.

6. M. Prosa, M. Bolognesi, L. Fornasari, et al., "Nanostructured Organic/Hybrid Materials and Components in Miniaturized Optical and Chemical Sensors," *Nanomaterials* 10 (2020): 480, https://doi.org/10.3390/nano10030480.

7. M. Prosa, E. Benvenuti, D. Kallweit, et al., "Organic Light-Emitting Transistors in a Smart-Integrated System for Plasmonic-Based Sensing," *Advanced Functional Materials* 31 (2021): 2104927, https://doi.org/10.1002/adfm.202104927.

8. D. Yuan, V. Sharapov, X. Liu, and L. Yu, "Design of High-Performance Organic Light-Emitting Transistors," *ACS Omega* 5 (2020): 68–74, https://doi.org/10.1021/acsomega.9b03630.

9. F. Reginato, E. Lunedei, S. Mattiello, et al., "Improved Charge Recombination Efficiency in Organic Light-Emitting Transistors via Luminescent Radicals," *Advanced Functional Materials* 35 (2025): 2411845, https://doi.org/10.1002/adfm.202411845.

10. S. Moschetto, B. M. Squeo, F. Reginato, M. Prosa, M. Pasini, and S. Toffanin, "A Fluorescent Conjugated Polar Polymer for Probing Charge Injection in Multilayer Organic Light-Emitting Transistors," *Molecules (Basel, Switzerland)* 29 (2024): 3295, https://doi.org/10.3390/molecules29143295.

11. M. Zambianchi, E. Benvenuti, C. Bettini, et al., "Anthracene-Based Molecular Emitters for Non-doped Deep-blue Organic Light Emitting Transistors," *Journal of Materials Chemistry C* 4 (2016): 9411–9417, https://doi.org/10.1039/c6tc02949c.

12. D. Yuan, M. A. Awais, V. Sharapov, et al., "Foldable Semi-Ladder Polymers: Novel Aggregation Behavior and High-Performance Solution-Processed Organic Light-Emitting Transistors," *Chemical Science* 11 (2020): 11315–11321, https://doi.org/10.1039/d0sc04068a.

13. S. Mecca, F. Pallini, V. Pinchetti, et al., "Multigram-Scale Synthesis of Luminescent Cesium Lead Halide Perovskite Nanobricks for Plastic Scintillators," *ACS Applied Nano Materials* 6 (2023): 9436–9443, https://doi.org/10.1021/acsanm.3c01146.

14. S. Wang, A. A. Yousefi Amin, L. Wu, M. Cao, Q. Zhang, and T. Ameri, "Perovskite Nanocrystals: Synthesis, Stability, and Optoelectronic Applications," *Small Structures* 2 (2021): 2000124, https://doi.org/10.1002/sstr.202000124.

15. A. Dey, J. Ye, A. De, et al., "State of the Art and Prospects for Halide Perovskite Nanocrystals," *ACS Nano* 15 (2021): 10775–10981, https://doi.org/10.1021/acsnano.0c08903.

16. L. Protesescu, S. Yakunin, M. I. Bodnarchuk, et al., "Nanocrystals of Cesium Lead Halide Perovskites ($CsPbX_3$, X = Cl, Br, and I): Novel Optoelectronic Materials Showing Bright Emission With Wide Color Gamut," *Nano Letters* 15 (2015): 3692–3696, https://doi.org/10.1021/nl5048779.

17. H. Huang, L. Polavarapu, J. A. Sichert, A. S. Susha, A. S. Urban, and A. L. Rogach, "Colloidal Lead Halide Perovskite Nanocrystals: Synthesis, Optical Properties and Applications," *NPG Asia Materials* 8 (2016): e328–e328, https://doi.org/10.1038/am.2016.167.

18. J. S. Kim, J. M. Heo, G. S. Park, et al., "Ultra-Bright, Efficient and Stable Perovskite Light-Emitting Diodes," *Nature* 611 (2022): 688–694, https://doi.org/10.1038/s41586-022-05304-w.

19. X. Liu, X. Guo, Y. Lv, et al., "High Brightness and Enhanced Stability of $CsPbBr_3$-Based Perovskite Light-Emitting Diodes by Morphology and Interface Engineering," *Advanced Optical Materials* 6 (2018): 1801245, https://doi.org/10.1002/adom.201801245.

20. D. Yang, B. Zhao, T. Yang, et al., "Toward Stable and Efficient Perovskite Light-Emitting Diodes," *Advanced Functional Materials* 32 (2022): 2109495, https://doi.org/10.1002/adfm.202109495.

21. Z. Li, Q. Wei, Y. Wang, et al., "Highly Bright Perovskite Light-Emitting Diodes Enabled by Retarded Auger Recombination," *Nature Communications* 16 (2025): 927, https://doi.org/10.1038/s41467-025-56001-x.

22. L. Zhao, D. D. Astridge, W. B. Gunnarsson, et al., "Thermal Properties of Polymer Hole-Transport Layers Influence the Efficiency Roll-Off and Stability of Perovskite Light-Emitting Diodes," *Nano Letters* 23 (2023): 4785–4792, https://doi.org/10.1021/acs.nanolett.3c00148.

23. S.-D. Baek, W. Shao, W. Feng, et al., "Grain Engineering for Efficient Near-Infrared Perovskite Light-Emitting Diodes," *Nature Communications* 15 (2024): 10760, https://doi.org/10.1038/s41467-024-55075-3.

24. D. Xing, C. C. Lin, Y. L. Ho, et al., "Self-Healing Lithographic Patterning of Perovskite Nanocrystals for Large-Area Single-Mode Laser Array," *Advanced Functional Materials* 31 (2021): 2006283, https://doi.org/10.1002/adfm.202006283.

25. S. Zhou, G. Zhou, Y. Li, et al., "Understanding Charge Transport in All-Inorganic Halide Perovskite Nanocrystal Thin-Film Field Effect Transistors," *ACS Energy Letters* 5 (2020): 2614–2623, https://doi.org/10.1021/acsenergylett.0c01295.

26. D. K. Kim, D. Choi, M. Park, K. S. Jeong, and J. H. Choi, "Cesium Lead Bromide Quantum Dot Light-Emitting Field-Effect Transistors," *ACS Applied Materials & Interfaces* 12 (2020): 21944–21951, https://doi.org/10.1021/acsami.0c06904.

27. A. N. Aleshin, I. P. Shcherbakov, O. P. Chikalova-Luzina, et al., "Photo- and Electroluminescence Features of Films and Field Effect Transistors Based on Inorganic Perovskite Nanocrystals Embedded in a Polymer Matrix," *Synthetic Metals* 260 (2020): 116291, https://doi.org/10.1016/j.synthmet.2020.116291.

28. A. N. Aleshin, I. P. Shcherbakov, D. A. Kirilenko, L. B. Matyushkin, and V. A. Moshnikov, "Light-Emitting Field-Effect Transistors Based on Composite Films of Polyfluorene and $CsPbBr_3$ Nanocrystals," *Physics of the Solid State* 61 (2019): 256–262, https://doi.org/10.1134/S1063783419020021.

29. X. Zhang, M. Guo, J. Li, et al., "Enhanced Light-emitting Transistors Utilizing Multi-dimensional $CsPbBr_3$ Perovskite Films and PVP-Modified ZTO Semiconductor Layers," *Journal of Materials Chemistry C* 12 (2024): 14887–14892, https://doi.org/10.1039/d4tc03440f.

30. Y. J. Park, M. Kim, A. Song, et al., "Light-Emitting Transistors With High Color Purity Using Perovskite Quantum Dot Emitters," *ACS Applied Materials & Interfaces* 12 (2020): 35175–35180, https://doi.org/10.1021/acsami.0c05537.

31. X. Liu, D. Yu, X. Song, and H. Zeng, "Metal Halide Perovskites: Synthesis, Ion Migration, and Application in Field-Effect Transistors," *Small* 14 (2018): 1801460, https://doi.org/10.1002/smll.201801460.

32. M. Prosa, N. Li, N. Gasparini, et al., "Revealing Minor Electrical Losses in the Interconnecting Layers of Organic Tandem Solar Cells," *Advanced Materials Interfaces* 4 (2017): 1700776, https://doi.org/10.1002/admi.201700776.

33. H. Bouzid, M. Prosa, M. Bolognesi, et al., "Impact of Environmentally Friendly Processing Solvents on the Properties of Blade-Coated Polymer Solar Cells," *Journal of Polymer Science Part A: Polymer Chemistry* 57 (2019): 487–494, https://doi.org/10.1002/pola.29286.

34. L. Wang, B. Liu, X. Zhao, H. V. Demir, H. Gu, and H. Sun, "Solvent-Assisted Surface Engineering for High-Performance All-Inorganic Perovskite Nanocrystal Light-Emitting Diodes," *ACS Applied Materials & Interfaces* 10 (2018): 19828–19835, https://doi.org/10.1021/acsami.8b06105.

35. M. Ban, Y. Zou, J. P. H. Rivett, et al., "Solution-processed Perovskite Light Emitting Diodes With Efficiency Exceeding 15% Through Additive-Controlled Nanostructure Tailoring," *Nature Communications* 9 (2018): 3892, https://doi.org/10.1038/s41467-018-06425-5.

36. F. Chen, Y. Liu, and M. Salerno, "Dispersing Solvent Effect on Halide Perovskite Nanocrystals-Based Films and Devices," *Journal of Materials Science* 57 (2022): 1902–1913, https://doi.org/10.1007/s10853-021-06777-2.

37. S. N. Raja, Y. Bekenstein, M. A. Koc, et al., "Encapsulation of Perovskite Nanocrystals Into Macroscale Polymer Matrices: Enhanced Stability and Polarization," *ACS Applied Materials & Interfaces* 8 (2016): 35523–35533, https://doi.org/10.1021/acsami.6b09443.

38. K. S. Yook and J. Y. Lee, "Small Molecule Host Materials for Solution Processed Phosphorescent Organic Light-Emitting Diodes," *Advanced Materials* 26 (2014): 4218–4233, https://doi.org/10.1002/adma.201306266.

39. J. Li, Y. Zhao, H. S. Tan, et al., "A Stable Solution-processed Polymer Semiconductor With Record High-mobility for Printed Transistors," *Scientific Reports* 2 (2012): 754, https://doi.org/10.1038/srep00754.

40. A. Erroi, S. Mecca, M. L. Zaffalon, et al., "Ultrafast and Radiation-Hard Lead Halide Perovskite Nanocomposite Scintillators," *ACS Energy Letters* 8 (2023): 3883–3894, https://doi.org/10.1021/acsenergylett.3c01396.

41. V. Bellotti, F. Carulli, S. Mecca, et al., "Perovskite Nanocrystals Initiate One-Step Oxygen Tolerant PET-RAFT Polymerization of Highly Loaded, Efficient Plastic Nanocomposites," *Advanced Functional Materials* 34 (2024): 2411319, https://doi.org/10.1002/adfm.202411319.

42. Z. Liu, Y. Bekenstein, X. Ye, et al., "Ligand Mediated Transformation of Cesium Lead Bromide Perovskite Nanocrystals to Lead Depleted Cs_4PbBr_6 Nanocrystals," *Journal of the American Chemical Society* 139 (2017): 5309–5312, https://doi.org/10.1021/jacs.7b01409.

43. D. Guggisberg, S. Yakunin, C. Neff, et al., "Colloidal $CsPbX_3$ Nanocrystals With Thin Metal Oxide Gel Coatings," *Chemistry of Materials* 35 (2023): 2827–2834, https://doi.org/10.1021/acs.chemmater.2c03562.

44. X. Huang, G. Deng, S. Zhan, et al., "Solvent Gaming Chemistry to Control the Quality of Halide Perovskite Thin Films for Photovoltaics," *ACS Central Science* 8 (2022): 1008–1016, https://doi.org/10.1021/acscentsci.2c00385.

45. Z. Feng, L. Wang, H. Yu, et al., "Towards Efficient Perovskite Light-Emitting Diodes: A Multi-Step Spin-Coating Method for a Dense and Uniform Perovskite Film," *Organic Electronics* 61 (2018): 18–24, https://doi.org/10.1016/j.orgel.2018.06.052.

46. P. I. Shin, C. F. Shu, Y. L. Tung, and Y. Chi, "Efficient White-Light-Emitting Diodes Based on Poly(N-vinylcarbazole) Doped With Blue Fluorescent and Orange Phosphorescent Materials," *Applied Physics Letters* 88 (2006): 251110, https://doi.org/10.1063/1.2214141.

47. K. S. Bejoymohandas, A. Baschieri, F. Reginato, et al., "Stereoisomeric Homo- and Hetero-Binuclear Iridium(III) Complexes With 3-Oxidopicolinate Bridging Ligand and Their Application in OLEDs," *Advanced Optical Materials* 12 (2024): 2401586, https://doi.org/10.1002/adom.202401586.

48. G. Baroni, F. Reginato, M. Prosa, et al., "Photo-gain Optimization in Multilayer Organic Phototransistors by Study of Space-Charge Limited Current," *Journal of Materials Chemistry C* 12 (2024): 12962–12970, https://doi.org/10.1039/d4tc01925c.

49. H. Chen, X. Xing, J. Miao, et al., "Highly Efficient Flexible Organic Light Emitting Transistor Based on High- k Polymer Gate Dielectric," *Advanced Optical Materials* 8 (2020): 1901651, https://doi.org/10.1002/adom.201901651.

50. H. Ren, N. Cui, Q. Tang, Y. Tong, X. Zhao, and Y. Liu, "High-Performance, Ultrathin, Ultraflexible Organic Thin-Film Transistor Array

Via Solution Process," *Small* 14 (2018): 1801020, https://doi.org/10.1002/smll.201801020.

51. W. Wang, D. Ma, S. Pan, and Y. Yang, "Hysteresis Mechanism in Low-voltage and High Mobility Pentacene Thin-Film Transistors With Polyvinyl Alcohol Dielectric," *Applied Physics Letters* 101 (2012): 033303, https://doi.org/10.1063/1.4737173.

52. G. Baroni, F. Reginato, S. Mattiello, et al., "High-Sensitivity Solution-Processed Organic Phototransistor Based on a Bulk Heterojunction With a Persistent Radical as the Electron Acceptor," *ACS Applied Electronic Materials* 7 (2025): 3694–3703, https://doi.org/10.1021/acsaelm.4c02334.

53. M. Natali, M. Prosa, A. Longo, et al., "On the Nature of Charge-Injecting Contacts in Organic Field-Effect Transistors," *ACS Applied Materials & Interfaces* 12 (2020): 30616–30626, https://doi.org/10.1021/acsami.0c05106.

Supporting Information

Additional supporting information can be found online in the Supporting Information section.

Supporting File: aelm70318-sup-0001-SuppMat.docx.